

Model calculations

We used a one-proton radical-pair model<sup>28</sup> with an isotropic hyperfine coupling, *a*, of 0.5 mT, an anisotropy,  $\alpha$  of 0.3, and a lifetime of 20  $\mu$ s (corresponding to the observed lifetime of flavin-tryptophan radical pairs<sup>15</sup>). We solved the stochastic Liouville equation to determine the triplet yield in the presence of a static magnetic field of 46  $\mu$ T. We then calculated, by direct numerical integration of the stochastic Liouville equation, the change in triplet yield,  $\Delta\Phi_{\text{OMF}}$ , caused by an additional 1.3 MHz oscillating magnetic field in resonance with the splitting due to the 46  $\mu$ T static field. For comparison, we also calculated the triplet yield change,  $\Delta\Phi_{\text{static}}$ , resulting from a decrease of 12  $\mu$ T in static field, noting that such a change led to disorientation in the magnetic compass orientation responses of robins<sup>29</sup>. The intensity of the oscillating field required for  $\Delta\Phi_{\text{OMF}}$  to equal  $\Delta\Phi_{\text{static}}$  is 0.033  $\mu$ T, that is, less than any of the intensities employed in our experiments.

Received 2 September 2003; accepted 30 March 2004; doi:10.1038/nature02534.

1. Wiltschko, W. & Wiltschko, R. Magnetic compass of European robins. *Science* **176**, 62–64 (1972).
2. Wiltschko, R. & Wiltschko, W. *Magnetic Orientation in Animals* (Springer, Berlin, 1995).
3. Kirschvink, J. & Gould, J. Biogenic magnetite as a basis for magnetic field detection in animals. *BioSystems* **13**, 181–201 (1981).
4. Edmonds, D. T. A sensitive optically detected magnetic compass for animals. *Proc. R. Soc. Lond. B* **263**, 295–298 (1996).
5. Shcherbakov, V. P. & Winklhofer, M. The osmotic magnetometer: a new model for a magnetite-based magnetoreceptor in animals. *Eur. Biophys. J.* **28**, 380–392 (1999).
6. Leask, M. J. A physico-chemical mechanism for magnetic field detection by migratory birds and homing pigeons. *Nature* **267**, 144–145 (1977).
7. Schulten, K. Magnetic field effects in chemistry and biology. *Festkörperprobleme (Adv. Solid State Phys.)* **22**, 61–83 (1982).
8. Ritz, T., Adem, S. & Schulten, K. A photoreceptor-based model for magnetoreception in birds. *Biophys. J.* **78**, 707–718 (2000).
9. Wiltschko, W., Munro, U., Ford, H. & Wiltschko, R. Red light disrupts magnetic orientation of migratory birds. *Nature* **364**, 525–527 (1993).
10. Wiltschko, W. & Wiltschko, R. Magnetic compass orientation in birds and its physiological basis. *Naturwissenschaften* **89**, 445–452 (2002).
11. Wiltschko, W., Traudt, J., Güntürkün, O., Prior, H. & Wiltschko, R. Lateralization of magnetic compass orientation in a migratory bird. *Nature* **419**, 467–470 (2002).
12. Kobayashi, A. & Kirschvink, J. in *Electromagnetic Fields: Biological Interactions and Mechanisms* (ed. Blank, M.) 367–394 (American Chemical Society Books, Washington DC, 1995).
13. Weaver, J., Vaughn, T. & Astumian, R. Biological sensing of small differences by magnetically sensitive chemical reactions. *Nature* **405**, 707–709 (2000).
14. Kirschvink, J. *et al.* in *Sensory Transduction* (eds Corey, D. & Roper, S.) 225–240 (Society of General Physiologists 45th Annu. Symp., Rockefeller Univ. Press, New York, 1992).
15. Cintolesi, F., Ritz, T., Kay, C., Timmel, C. & Hore, P. Anisotropic recombination of an immobilized photoinduced radical pair in a 50  $\mu$ T magnetic field: a model avian photomagnetoreceptor. *Chem. Phys.* **294**, 384–399 (2003).
16. Wiltschko, W. & Wiltschko, R. The effect of yellow and blue light on magnetic compass orientation in European Robins, *Erithacus rubecula*. *J. Comp. Physiol. A* **184**, 295–299 (1999).
17. Wiltschko, W., Gesson, M. & Wiltschko, R. Magnetic compass orientation of European robins under 565 nm green light. *Naturwissenschaften* **88**, 387–390 (2001).
18. Canfield, J., Belford, R., Debrunner, P. & Schulten, K. A perturbation theory treatment of oscillating magnetic fields in the radical pair mechanism. *Chem. Phys.* **182**, 1–18 (1994).
19. Kirschvink, J. Microwave absorption by magnetite: a possible mechanism for coupling nonthermal levels of radiation to biological systems. *Bioelectromagnetics* **17**, 187–194 (1996).
20. Beason, R. C. & Nichols, J. E. Magnetic orientation and magnetically sensitive material in a transequatorial migratory bird. *Nature* **309**, 151–153 (1984).
21. Fleissner, G. *et al.* Ultrastructural analysis of a putative magnetoreceptor in the beak of homing pigeons. *J. Comp. Neurol.* **458**, 350–360 (2003).
22. Beason, R. & Semm, P. Does the ophthalmic nerve carry magnetic navigational information? *J. Exp. Biol.* **199**, 1241–1244 (1996).
23. Munro, U., Munro, J. A., Phillips, J. B., Wiltschko, R. & Wiltschko, W. Evidence for a magnetite-based navigational 'map' in birds. *Naturwissenschaften* **84**, 26–28 (1997).
24. Wiltschko, W., Munro, U., Ford, H. & Wiltschko, R. Effect of a magnetic pulse on the orientation of silvereyes, *Zosterops l. lateralis*, during spring migration. *J. Exp. Biol.* **201**, 3257–3261 (1998).
25. Semm, P. & Beason, R. C. Responses to small magnetic variations by the trigeminal system of the bobolink. *Brain Res. Bull.* **25**, 735–740 (1990).
26. Beason, R. C. & Semm, P. in *Acta XX Congr. Int. Ornithol.* (ed. Bell, B. D.) 1813–1819 (New Zealand Ornithol. Congr. Trust Board, Wellington, 1991).
27. Batschelet, E. *Circular Statistics in Biology* (Academic, London, 1981).
28. Timmel, C., Cintolesi, F., Brocklehurst, B. & Hore, P. Model calculations of magnetic field effects on the recombination reactions of radicals with anisotropic hyperfine interactions. *Chem. Phys. Lett.* **334**, 387–395 (2001).
29. Wiltschko, W. in *Animal Migration, Navigation and Homing* (eds Koenig, K. & Keeton, W.) 302–310 (Springer, Berlin, 1978).

**Acknowledgements** We thank the Deutsche Telekom AG, especially H. Küpper, T. Loppnow and B. Marx for technical assistance, and F. Galera, S. Hilmer, C. Koschella and S. Münzner for their help with conducting the experiments. J.B.P. acknowledges the National Science Foundation for financial support. Our work was supported by the Deutsche Forschungsgemeinschaft (W.W.) and the Fetzer Institute (T.R.).

**Competing interests statement** The authors declare that they have no competing financial interests.

**Correspondence** and requests for materials should be addressed to T.R. (tritz@uci.edu).

Modelling disease outbreaks in realistic urban social networks

Stephen Eubank<sup>1</sup>, Hasan Guclu<sup>2</sup>, V. S. Anil Kumar<sup>1</sup>, Madhav V. Marathe<sup>1</sup>, Aravind Srinivasan<sup>3</sup>, Zoltán Toroczkai<sup>4</sup> & Nan Wang<sup>5</sup>

<sup>1</sup>Basic and Applied Simulation Science Group, Los Alamos National Laboratory, MS M997, Los Alamos, New Mexico 87545, USA

<sup>2</sup>Department of Physics, Applied Physics and Astronomy, Rensselaer Polytechnic Institute 110 8th Street, Troy, New York 12180-3590, USA

<sup>3</sup>Department of Computer Science and Institute for Advanced Computer Studies, University of Maryland, College Park, Maryland 20742, USA

<sup>4</sup>Centre for Nonlinear Studies and Complex Systems Group, Los Alamos National Laboratory, MS B258, Los Alamos, New Mexico 87545, USA

<sup>5</sup>Department of Computer Science, University of Maryland, College Park, Maryland 20742, USA

Most mathematical models for the spread of disease use differential equations based on uniform mixing assumptions<sup>1</sup> or *ad hoc* models for the contact process<sup>2–4</sup>. Here we explore the use of dynamic bipartite graphs to model the physical contact patterns that result from movements of individuals between specific locations. The graphs are generated by large-scale individual-based urban traffic simulations built on actual census, land-use and population-mobility data. We find that the contact network among people is a strongly connected small-world-like<sup>5</sup> graph with a well-defined scale for the degree distribution. However, the locations graph is scale-free<sup>6</sup>, which allows highly efficient outbreak detection by placing sensors in the hubs of the locations network. Within this large-scale simulation framework, we then analyse the relative merits of several proposed mitigation strategies for smallpox spread. Our results suggest that outbreaks can be contained by a strategy of targeted vaccination combined with early detection without resorting to mass vaccination of a population.

The dense social-contact networks characteristic of urban areas form a perfect fabric for fast, uncontrolled disease propagation. Current explosive trends in urbanization exacerbate the problem: it is estimated that by 2030 more than 60% of the world's population will live in cities<sup>7</sup>. This raises important questions, such as: How can an outbreak be contained before it becomes an epidemic, and what disease surveillance strategies should be implemented? Recent studies<sup>1</sup>, under the assumption of homogeneous mixing, make the case for mass vaccination in response to a smallpox outbreak. With different assumptions, it has been shown<sup>2</sup> that mass vaccination is not required. Policymakers must trade off the risks associated with vaccinating a large population<sup>8</sup> against the poorly understood risks of losing control of an outbreak. Addressing such specific policy questions<sup>9</sup> requires a higher-resolution description of disease spread than that offered by the homogeneous-mixing assumption and the differential-equations approach.

Here we present a highly resolved agent-based simulation tool (EpiSims), which combines realistic estimates of population mobility, based on census and land-use data, with parameterized models for simulating the progress of a disease within a host and of transmission between hosts<sup>10</sup>. The simulation generates a large-scale, dynamic contact graph that replaces the differential equations of the classic approach. EpiSims is based on the Transportation Analysis and Simulation System (TRANSIMS) developed at Los Alamos National Laboratory, which produces estimates of social networks based on the assumption that the transportation infrastructure constrains people's choices about where and when to perform activities<sup>11</sup>. TRANSIMS creates a synthetic population endowed with demographics such as age and income, consistent with joint distributions in census data. It then estimates positions

and activities of all travellers on a second-by-second basis. For more information on TRANSIMS and its availability, see Supplementary Information. The resulting social network is the best extant estimate of the physical contact patterns among large groups of people—alternative methodologies are limited to physical contacts among hundreds of people or non-physical contacts (such as e-mail or citations) among large groups.

The case study we present is a model of Portland, Oregon, USA, but the approach is broadly applicable. People, in the course of carrying out their daily activities (such as work, study or shopping), move between several locations, both exposing themselves to infectious agents within these locations and transporting those agents between locations. We represent these processes by a social contact network, which can be represented as a bipartite graph,  $G_{PL}$ , as shown by the example in Fig. 1a. For Portland,  $G_{PL}$  has about 1.6 million vertices, with a giant component of about 1.5 million people and 180,000 locations. The degree distribution of the people vertices in  $G_{PL}$ , that is, the number of people  $Q_j^{PL}$  who visited  $j$  different locations, is shown in Fig. 2a. It has a sharp peak near the average value of about four different locations, followed by a fast, exponentially decaying tail. The degree distribution for the location vertices in  $G_{PL}$  is very different, as shown in Fig. 2b. This is the number of locations  $M_i^{PL}$  having  $i$  different visitors during the day. The distribution has a power-law tail with an exponent of about  $-2.8$ .

For many infectious diseases, transmission occurs mainly between people who are collocated (simultaneously in the same

location), and spread is due mainly to people's movement. Hence we look at two natural projections of  $G_{PL}$  obtained by drawing an edge between all pairs of vertices distance two from each other on the bipartite graph, as illustrated in Fig. 1b, c. The result is two disconnected graphs:  $G_P$ , containing only people vertices, and  $G_L$ , containing only locations. In  $G_P$ , the edges are labelled with the sets of time intervals during which the people were collocated. For simplicity, however, we consider  $\hat{G}_P$ , a static projection of the time-resolved  $G_P$ , obtained by discarding time labels, as shown in Fig. 1d. This is reasonable for diseases such as smallpox, severe acute respiratory syndrome or influenza, in which both the incubation period and duration of infectivity are of the order of several days, much longer than the 24-h approximate periodicity of people's contacts. This assumption introduces a systematic bias into results based on  $\hat{G}_P$ : the static projection yields a worst-case scenario of how the disease is likely to propagate, because  $\hat{G}_P$  is much more connected than  $G_P$ . Any control strategy that is effective in such worst-case scenarios will also be effective in the time-resolved case. Furthermore, we have modelled the idea of an effective contact (one in which the transmission of disease is likely to occur) by removing from  $\hat{G}_P$  all edges for which the duration of contact was less than some minimum threshold, usually one hour. Even this thresholded version of  $\hat{G}_P$  is biased towards more connectivity than  $G_P$ . An alternative to thresholding is to weight edges according to duration (and other factors affecting transmission). Figure 2c shows the degree distribution of  $\hat{G}_P$  for the Portland network. The other important projection of the bipartite graph is the locations network  $G_L$ . If there is at least one person travelling from location  $l_1$  directly to  $l_2$  during the day, the two vertices corresponding to locations  $l_1$  and  $l_2$  are connected by a directed edge in  $G_L$  from  $l_1$  to  $l_2$  that indicates whether the person is travelling in or out of the location. As before, we form a static version of the locations network,  $\hat{G}_L$ , by ignoring the time labels on the edges. The in and out degree distributions for the locations network are superimposed in Fig. 2d (ref. 12). The power-law decay evident there shows that  $\hat{G}_L$  is a scale-free network<sup>6</sup> with an exponent of  $\gamma \sim -2.8$ . A simple explanation for this empirical observation is based on the capacity

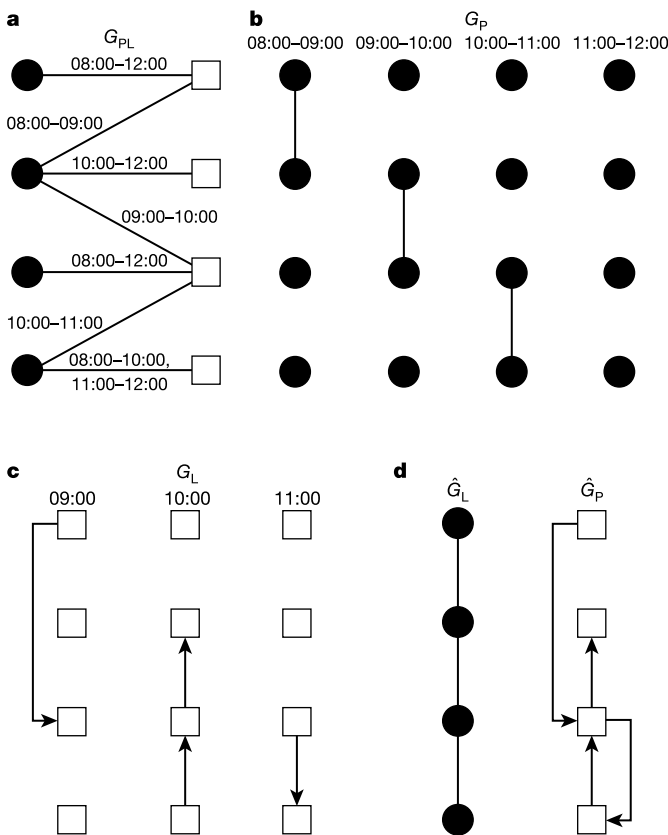


**Figure 1** An example of a small social contact network. **a**, A bipartite graph  $G_{PL}$  with two types of vertex representing four people ( $P$ ) and four locations ( $L$ ). If person  $p$  visited location  $l$ , there is an edge in this graph between  $p$  and  $l$ . Vertices are labelled with appropriate demographic or geographic information, edges with arrival and departure times. **b**, **c**, The two disconnected graphs  $G_P$  and  $G_L$  induced by connecting vertices that were separated by exactly two edges in  $G_{PL}$ . **d**, The static projections  $\hat{G}_P$  and  $\hat{G}_L$  resulting from ignoring time labels in  $G_P$  and  $G_L$ . People (such as 24-year-old male) are represented by filled circles, and locations (such as 34 Elm Street) by open squares.

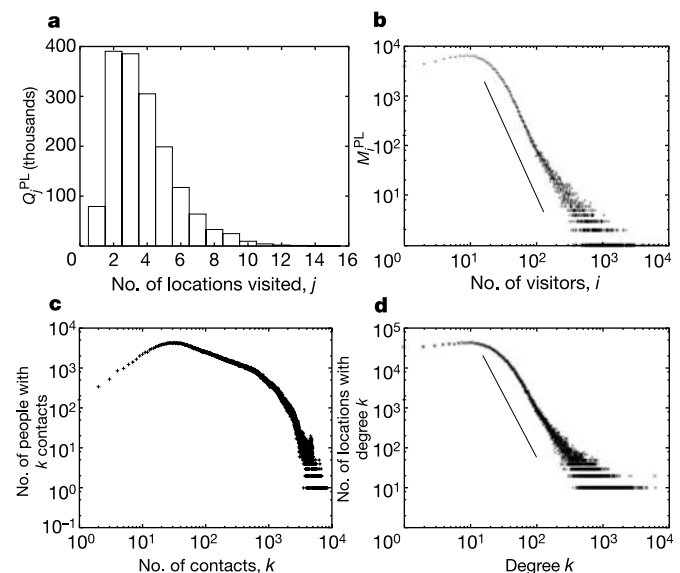


**Figure 2** Degree distributions for the estimated Portland social network. **a**, The number of people  $Q_j^{PL}$  who visited  $j$  different locations in the bipartite people–locations graph  $G_{PL}$ . **b**, The number of locations  $M_i^{PL}$  in  $G_{PL}$  that are visited by exactly  $i$  different people. The slope of the straight-line graph is  $-2.8$ . **c**, The number of people who have  $k$  neighbours in the static people–contact graph  $\hat{G}_P$  on log–log scale. **d**, The in and out degree distributions of the locations network  $\hat{G}_L$ . The slope of the straight-line graph is  $-2.8$ .

distribution of the locations in Portland. Land-use data indicate that the number of people using a location (its capacity) follows a power-law distribution with the same exponent  $\gamma$ . In large urban areas, people tend to fill locations up to their capacity. More densely filled locations (for example shopping malls) will have a larger number of people moving in from a proportionally larger number of other different locations (for example, homes), which in turn generates the scale-free character of  $\hat{G}_L$  with the capacity exponent  $\gamma$ .

Measurements of the average clustering coefficient (see Methods) for  $\hat{G}_P$  yield  $C_P \approx 0.48$ , and for  $\hat{G}_L$ ,  $C_L \approx 0.04$ , both much larger than the roughly  $10^{-6}$  of an Erdős–Rényi random graph with the same number of vertices and average degree<sup>5</sup>. This, together with the degree distribution and its small diameter (about 6), suggests that the people-contact graph is more like a small-world graph<sup>5</sup> than a random graph. The clustering coefficient distributions versus degree<sup>13,14</sup> shown in Supplementary Fig. 1 indicate that the locations network  $\hat{G}_L$  is an empirical example of a hierarchical scale-free structure<sup>15–17</sup>.

Both degree distribution and clustering are relevant to short-term propagation in a network, but longer time dynamics will be driven by global graph properties. It is thus natural to consider estimation schemes for global topological measures, such as expansion (see Methods). Informally, the higher the expansion, the quicker is the spread of any phenomenon (such as disease, gossip or data). We estimated an expansion value of about 2 for  $G_P$  by random sampling, indicating that the people-contact graph is extremely connected. An immediate consequence is that, as for an assortatively mixed network<sup>18</sup>,  $\hat{G}_P$  cannot be shattered by removing (by means of vaccination or quarantine) a small number of high-degree vertices<sup>19–22</sup>. To verify this, we have computed the size of the giant component—the maximum number of people at risk for disease introduced by a single person—when all vertices of degree more than  $k$  are removed. A unique giant component persists even when all vertices of degree 11 and higher are removed, as shown in Fig. 3a. Thus, attempting to shatter the contact graph by vaccinating the most gregarious people in a population would essentially be equivalent to mass vaccination. Similarly, we show in Fig. 3b, c

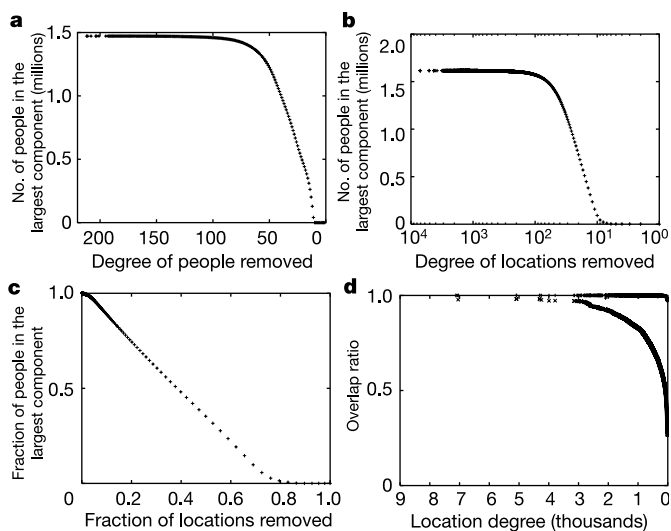


**Figure 3** Shattering and covering the people-contact graph. In **a** we remove (by vaccination or quarantine) all people with degree  $k$  and higher from the bipartite graph  $G_{PL}$ . In **b** and **c** we remove all locations with degree  $k$  or higher from  $G_{PL}$  and monitor the size of the largest connected component in the static people-contact graph induced by the remaining bipartite graph. **d**, Overlap ratios by degree. The lower curve shows the cumulative overlap ratio by degree, which is the overlap ratio for locations having degree  $k$  or less. The upper curve shows the overlap ratio for locations having degree exactly  $k$ .

that closing the most-visited locations—or vaccinating everyone who visits them—does not shatter the induced people-contact graph until large fractions of the population have been affected. Other infrastructure networks exhibit very different shattering properties.

Can epidemics be stopped without resorting to mass vaccination? Alternatives rely on early detection and efficient targeting. Here we introduce the overlap ratio, another non-local property of the graph that is crucial to early detection. Consider an idealized situation in which sensors at a location can detect whether any person there is infected. The feasibility of early detection depends on the number of sensors required to cover the population. This problem is equivalent to finding the minimum dominating set<sup>23</sup>. That is, we wish to find a subset  $L'$  of locations so that all (or most) people visit some location in  $L'$ . The overlap ratio<sup>23</sup>  $\omega(J)$  of a set of locations  $J \subset L$  is  $n(J) / \sum_{l \in J} \text{deg}(l)$ , where  $n(J)$  is the total number of people visiting any location in  $J$ , and  $\text{deg}(l)$  is the number of different people visiting location  $l \in J$ . The smaller the overlap ratio, the larger is the number of different locations in  $J$  visited by a single person. The overlap ratio by degree, shown in Fig. 3d, is the overlap ratio for the set  $J_k$  of locations having degree  $k$ . Clearly, not many people visit more than one high-degree location, which implies that the high-degree location vertices form a near-optimal dominating set. With high probability, early identification could be accomplished by using sensors placed at locations with the highest degree.

Alternatives to mass vaccination involve isolating and/or vaccinating small subsets of individuals to ensure that the disease will spread only locally in the graph. Most such strategies assume that people contacted by infectious people are the best candidates for vaccination or quarantine. However, it might also be possible to identify a good subset of the population to target before an outbreak.  $G_P$  is composed of tight-knit communities joined by long-range edges. A model for this structure is given by adding long-range edges to random geometric graphs<sup>24</sup>. An infectious individual (even one with low degree) who travels can nucleate two independent growth centres. Other long-range travellers near these centres can in turn nucleate an exponentially growing number of growth centres, as demonstrated by the rapid worldwide spread of severe acute respiratory syndrome. Thus, targeting long-distance travellers (say, across town for urban regions) is a crucial component of any response.

Our results on the expansion property indicate that disease is likely to spread quickly if not controlled early enough. However, exactly how the number of casualties depends on response delay and

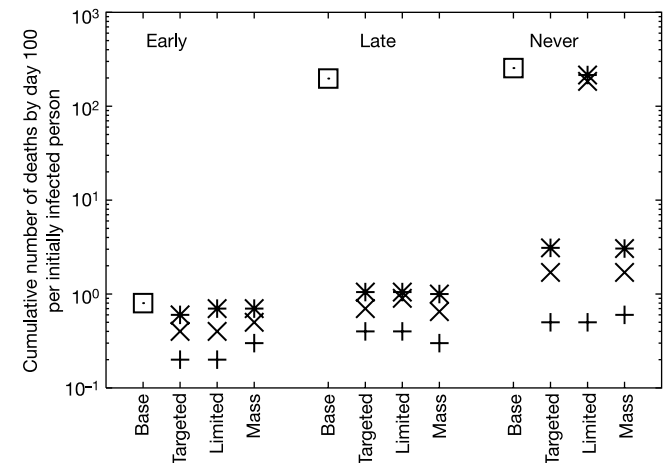


**Figure 4** Cumulative number of deaths per number of initial infected, for the case of a smallpox outbreak in downtown Portland, under a number of different response strategies: squares, no vaccine; stars, 10-day delay; multiplication signs, 7-day delay; plus signs, 4-day delay.

what constitutes ‘early enough’ depend on disease-specific factors such as incubation period and probability of transmission, as well as scenario-specific factors such as the means of introduction. Because these dependences cannot be easily determined from an analysis of the static social network, we turn to simulation, which captures the full time-dependence of  $G_{PL}$  (see Supplementary Methods for details).

There is not yet a consensus on models of smallpox. We have designed a model that captures many features on which there is widespread agreement<sup>9,25</sup> and allows us to vary poorly understood properties through reasonable ranges<sup>1,2,26</sup>. Our model includes the following features: the incubation period is a gaussian truncated at 7 and 17 days with a 12-day mean and 2-day deviation; the prodromal period is 3–5 days; the infectious period is 4 days, during which infectivity decreases exponentially; death occurs 10–16 days after the rash develops in 30% of normal cases. Ninety-five per cent of susceptibles exposed for 3 h to a person at minimum infectivity will become infected (the remaining 5% have extremely high or low susceptibilities, mimicking some anecdotal transmission incidents); vaccination is assumed to be 100% effective before exposure, and it reduces the mortality and transmission rates when administered up to 2 days after exposure (or 4 days for a previously vaccinated person, assumed to be everyone over the age of 30 years). The model also includes haemorrhagic variants with a shorter incubation period that are 10-fold as infectious and invariably fatal (see Methods and Supplementary Information for details).

Note that EpiSims does not specify a value for  $R_0$ , the basic reproductive number<sup>27</sup>. This parameter reflects how many people in a susceptible population are directly infected by the introduction of a single infective.  $R_0$  is a convolution of transmission rates and contact patterns, and EpiSims performs the convolution for us. The implied value of  $R_0$  is the ratio of the numbers of people in the first and original cohorts; that is, the number of people initially infected and the number infected directly by them. These estimates obviously include the effects of the simulated response strategy. For the set of experiments reported below,  $R_0$  ranges from 0.4 to 3.4.

In these scenarios, aerosolized smallpox was distributed indoors at busy locations over several hours, infecting of the order of 1,000 people. We assumed that the presence of smallpox was detected on the tenth day after the attack. Furthermore, we assumed that cases could be recognized in the prodromal phase after this date. We did not consider the confounding background distribution of influenza-like symptoms.

We studied the sensitivity of the number of casualties to three factors: mitigation efforts, delay in implementing mitigation efforts, and whether people move about while infectious. We simulated a passive (do nothing) ‘baseline’ and three active responses: mass vaccination covering 100% of the population in 4 days (‘mass’); targeted vaccination and quarantine with unlimited resources (‘targeted’); and the same targeted response, using only half as many contact tracers and vaccinators (‘limited’).

For a movie showing the spatial spread of disease under two different response strategies, see Supplementary Information. Figure 4 compares the efficacy of these strategies. For each strategy we plot (on a logarithmic scale) the ratio of the cumulative number of deaths by day 100 to the number initially infected. The absolute numbers are less important than the rank and relative sizes of gaps between the points. Also shown are the effects of delays of 4, 7 or 10 days in implementing the response. For each of the responses including the baseline, we allowed infected people to isolate themselves by withdrawing to the home. This could be due either to the natural history of the disease, which incapacitates its victims, or to actions taken by public health officials encouraging people to stay home. The results are grouped according to time of withdrawal to the home: (1) early, in which everyone withdraws before becoming infectious, producing the lowest estimates for  $R_0$ ; (2) late, in which everyone withdraws about 24 h after becoming infectious;

and (3) never, in which everyone carries on their daily activities unless they die. The extreme cases are unrealistic but are shown here because they demonstrate the existence of a clear transition.

In this study, time of withdrawal to the home is by far the most important factor, followed by delay in response. This indicates that targeted vaccination is feasible when combined with fast detection. Ironically, the actual strategy used is much less important than either of these factors. □

## Methods

### Clustering

Here we used the definition of the clustering coefficient,  $c_i = 2n_i/[k_i(k_i - 1)]$ , given in ref. 5, which measures the extent to which neighbours of a vertex are connected by edges ( $n_i$  is the number of connections between the neighbours of vertex  $i$ , and  $k_i$  is the degree of  $i$ ). Clustering has important implications for the rate and probability of disease spread<sup>4,28</sup>.

### Graph expansion

The vertex expansion of a set  $P' \subset P$  is the ratio between the number of distinct vertices not in  $P'$  reached through edges emanating from  $P'$  and the number of vertices in  $P'$ , denoted by  $|P'|$ . Clearly, the vertex expansion of a set  $P'$  with size  $|P'| = \alpha|P|$  is bounded above by  $\alpha^{-1} - 1$ . By definition, the vertex expansion of the graph  $G_P$  is the minimum of the vertex expansions of all sets  $P'$  with  $|P'| \leq N_P/2$ .

### Haemorrhagic variants

In our model, haemorrhagic variants occur in 20% of pregnant women, 10% of HIV-positive people, and 2.4% of the population at large. Of those, 30% get an ‘early haemorrhagic’ variant, with a prodromal period between 0.5 and 1.5 days and an infectious period of 1 day (until death). Pregnancy and HIV status are assigned on the basis of demographics.

### Simulation protocol

The protocol we simulated for targeted strategies was to place each prodromal person on a list. Contact tracers chose people at random from the list as they became available. We allowed 24 h for each contact tracer to vaccinate everyone living at the infected person’s home and to travel to each location that the infected person visited, vaccinating a fraction of the people there who had been present when the infected person was there. We varied the fraction vaccinated according to the type of activity, from zero at a shopping location to unity at work and home. After 24 h the contact tracer was freed to service the list again. The infected person was sent to a quarantine location. In the ‘targeted’ case, roughly 20 people were vaccinated for each person initially infected. The peak rate was 10 people per day per initial victim, or roughly 10,000 people per day.

Received 26 November 2003; accepted 5 April 2004; doi:10.1038/nature02541.

1. Kaplan, E., Craft, D. & Wein, L. Emergency response to a smallpox attack: the case for mass vaccination. *Proc. Natl Acad. Sci. USA* **99**, 10935–10940 (2002).
2. Halloran, M., Longini, I. M. Jr, Nizam, A. & Yang, Y. Containing bioterrorist smallpox. *Science* **298**, 1428–1432 (2002).
3. Kretzschmar, M. & Morris, M. Measures of concurrency in networks and the spread of infectious disease. *Math. Biosci.* **133**, 165–195 (1996).
4. Keeling, M. The effects of local spatial structure on epidemiological invasions. *Proc. R. Soc. Lond. B* **266**, 859–867 (1999).
5. Watts, D. & Strogatz, S. Collective dynamics of small-world networks. *Nature* **393**, 440–442 (1998).
6. Albert, R. & Barabási, A.-L. Statistical mechanics of complex networks. *Rev. Mod. Phys.* **74**, 47–97 (2002).
7. Zwingle, E. Megacities. *Natl Geogr. Mag.* **202**, 70–99 (2002).
8. Neff, J. M., Lane, J. M., Fulginiti, V. A. & Henderson, D. A. Contact vaccinia: transmission of vaccinia from smallpox vaccination. *J. Am. Med. Assoc.* **288**, 1901–1905 (2002).
9. Ferguson, N. et al. Planning for smallpox outbreaks. *Nature* **425**, 681–685 (2003).
10. Eubank, S. in *Proc. ACM Symp. Appl. Comput.* (eds Maniatty, W. & Szymanski, B.) 139–145 (ACM Press, New York, 2002).
11. Barrett, C. L. et al. *TRANSIMS: Transportation Analysis Simulation System* (Technical Report LA-UR-00-1725, Los Alamos National Laboratory, 2000).
12. Chowell, G., Hyman, J. M., Eubank, S. & Castillo-Chavez, C. Scaling laws for the movement of people between locations in a large city. *Phys. Rev. E* **68**, 066102 (2003).
13. Dorogovtsev, S. N., Goltsev, A. V. & Mendes, J. F. F. Pseudo-fractal scale-free web. *Phys. Rev. E* **65**, 066122 (2002).
14. Szabó, G., Alava, M. & Kertész, J. Structural transitions in scale-free networks. *Phys. Rev. E* **67**, 056102 (2003).
15. Jin, E., Girvan, M. & Newman, M. Structure of growing networks. *Phys. Rev. E* **64**, 046132 (2001).
16. Ravasz, E., Somera, A., Mongru, D., Oltvai, Z. & Barabási, A.-L. Hierarchical organization of modularity in metabolic networks. *Science* **297**, 1551–1555 (2002).
17. Albert, R., Jeong, H. & Barabási, A.-L. Error and attack tolerance of complex networks. *Nature* **406**, 378–382 (2000).
18. Newman, M. Assortative mixing in networks. *Phys. Rev. Lett.* **89**, 208701 (2002).
19. Pastor-Satorras, R. & Vespignani, A. Immunization of complex networks. *Phys. Rev. E* **65**, 036104 (2002).
20. Lloyd, A. & May, R. How viruses spread among computers and people. *Science* **292**, 1316–1317 (2001).
21. Callaway, C., Newman, M., Strogatz, S. & Watts, D. Network robustness and fragility: percolation on random graphs. *Phys. Rev. Lett.* **85**, 5468–5471 (2000).

22. Cohen, R., Erez, K., ben Avraham, D. & Havlin, S. Breakdown of the internet under intentional attack. *Phys. Rev. Lett.* **86**, 3682–3685 (2001).
23. Eubank, S., Anil Kumar, V., Marathe, M. V., Srinivasan, A. & Wang, N. in *Proc. ACM-SIAM Symp. Discrete Algorithms* (ed Munro, I.) 711–720 (SIAM Press, Philadelphia, 2004).
24. Dall, J. & Christensen, M. Random geometric graphs. *Phys. Rev. E* **66**, 016121 (2002).
25. Fenner, F., Henderson, D., Arita, I., Jezek, Z. & Ladnyi, I. *Smallpox and its Eradication* (World Health Organization, Geneva, 1988).
26. Eichner, M. & Dietz, K. Transmission potential of smallpox: estimates based on detailed data from an outbreak. *Am. J. Epidemiol.* **158**, 110–117 (2003).
27. Keeling, M. & Grenfell, B. T. Individual-based perspectives on  $R_0$ . *J. Theor. Biol.* **203**, 51–61 (2000).
28. Newman, M., Strogatz, S. & Watts, D. Properties of highly clustered networks. *Phys. Rev. E* **68**, 026121 (2003).

Supplementary Information accompanies the paper on [www.nature.com/nature](http://www.nature.com/nature).

**Acknowledgements** We thank G. Korniss, G. Istrate and the Fogarty International Center at the National Institutes of Health for useful discussions, and acknowledge the work of all the members of the TRANSIMS and EpiSims team. The EpiSims project is funded by the National Infrastructure Simulation and Analysis Program (NISAC) at the Department of Homeland Security. The TRANSIMS project was funded by the Department of Transportation. H.G. was supported in part by the National Science Foundation (Division of Materials Research) and Z.T. by the Department of Energy. We thank the anonymous referees for their helpful suggestions.

**Competing interests statement** The authors declare that they have no competing financial interests.

**Correspondence** and requests for materials should be addressed to S.G.E. ([eubank@lanl.gov](mailto:eubank@lanl.gov)).

## Enhanced synaptic plasticity in newly generated granule cells of the adult hippocampus

Christoph Schmidt-Hieber, Peter Jonas & Josef Bischofberger

Physiologisches Institut der Universität Freiburg, D-79104 Freiburg, Germany

Neural stem cells in various regions of the vertebrate brain continuously generate neurons throughout life<sup>1–4</sup>. In the mammalian hippocampus, a region important for spatial and episodic memory<sup>5,6</sup>, thousands of new granule cells are produced per day<sup>7</sup>, with the exact number depending on environmental conditions and physical exercise<sup>1,8</sup>. The survival of these neurons is improved by learning and conversely learning may be promoted by neurogenesis<sup>8–10</sup>. Although it has been suggested that newly generated neurons may have specific properties to facilitate learning<sup>2,10,11</sup>, the cellular and synaptic mechanisms of plasticity in these neurons are largely unknown. Here we show that young granule cells in the adult hippocampus differ substantially from mature granule cells in both active and passive membrane properties. In young neurons, T-type  $\text{Ca}^{2+}$  channels can generate isolated  $\text{Ca}^{2+}$  spikes and boost fast  $\text{Na}^+$  action potentials, contributing to the induction of synaptic plasticity. Associative long-term potentiation can be induced more easily in young neurons than in mature neurons under identical conditions. Thus, newly generated neurons express unique mechanisms to facilitate synaptic plasticity, which may be important for the formation of new memories.

To identify newly generated granule cells in the adult hippocampus, we applied electrophysiological, morphological and immunocytochemical criteria. We made whole-cell recordings from neurons in the granule cell layer and determined the input resistance ( $R_{\text{in}}$ ), which is known to be characteristically different between young and mature neurons<sup>12</sup>. Subsequently, we examined the immunoreactivity for polysialic acid neural cell adhesion

molecule (PSA-NCAM), a marker for newly generated granule cells<sup>1,3,13,14</sup>, and the morphology of the dendritic tree (Fig. 1).

On the basis of the distribution of  $R_{\text{in}}$ , most cells fell into two categories, with mean  $R_{\text{in}}$  values of  $232 \pm 78 \text{ M}\Omega$  and  $4.5 \pm 1.9 \text{ G}\Omega$ , respectively (mean  $\pm$  s.d.; Fig. 1a, c, e). Cells with high  $R_{\text{in}}$  were exclusively encountered in the inner granule cell layer adjacent to the subgranular zone, where neural stem cells are located<sup>1</sup>. Cells with  $R_{\text{in}}$  below  $400 \text{ M}\Omega$  were immunonegative for PSA-NCAM and showed a complex apical dendritic tree (total dendritic length  $3,652 \pm 134 \mu\text{m}$ ; mean  $\pm$  s.e.m.;  $n = 14$ ), indicating that they were mature granule cells. In contrast, all cells with  $R_{\text{in}}$  larger than  $1.5 \text{ G}\Omega$  were immunopositive for PSA-NCAM (Fig. 1d, f; relative fluorescence intensity  $76 \pm 6\%$ ) and had rudimentary apical and basal dendrites (Fig. 1f; total dendritic length  $845 \pm 111 \mu\text{m}$ ,  $n = 14$ ), indicative of immature granule cells<sup>15–17</sup>. As PSA-NCAM is expressed transiently in granule cells 1–3 weeks after mitosis<sup>13,14</sup>, these results suggest that the cells with high  $R_{\text{in}}$  are newly generated immature granule cells in the adult hippocampus. Cells with  $R_{\text{in}}$  larger than  $1.5 \text{ G}\Omega$  were immunonegative for parvalbumin ( $n = 4$ ), suggesting that they do not represent interneurons<sup>18,19</sup>.

We next studied the active and passive membrane properties of the two classes of neurons (Fig. 2). Both mature and young granule cells showed comparable resting potentials ( $-80.8 \pm 0.9 \text{ mV}$  versus  $-75.3 \pm 2.0 \text{ mV}$ , respectively) and were able to generate fast action potentials with large amplitudes (Fig. 2a–d;  $140 \pm 2 \text{ mV}$ ,  $n = 9$  versus  $115 \pm 2 \text{ mV}$ ,  $n = 6$ ). Unlike mature granule cells, which generated trains of action potentials during long current pulses (Fig. 2a; mean action potential frequency  $30 \pm 1 \text{ Hz}$ ), young neurons fired only a few action potentials per stimulus: in 15 of 20 cells, a single action potential was evoked (Fig. 2b). However, the current threshold determined with 100-ms pulses was markedly lower in young neurons than in mature cells ( $34 \pm 9 \text{ pA}$ ,  $n = 6$  versus  $141 \pm 12 \text{ pA}$ ,  $n = 4$ , respectively;  $P < 0.01$ ). In a subset of young neurons currents of less than  $10 \text{ pA}$  were sufficient to elicit an action potential. Finally, young neurons had a much slower membrane time constant,  $\tau_{\text{m}}$ , than mature granule cells (Fig. 2e, f;  $123 \pm 10 \text{ ms}$ ,  $n = 7$  versus  $54 \pm 4 \text{ ms}$ ,  $n = 13$ , respectively)<sup>20</sup>. Thus, newly generated granule cells have membrane properties that favour action potential generation with very small current stimuli, such as the opening of less than ten glutamate receptor channels<sup>21</sup>.

In contrast with mature neurons, young neurons generated transient low-threshold spikes when current injections below the threshold for  $\text{Na}^+$  action potential initiation were applied (Figs 2b and 3). Low-threshold spikes were insensitive to  $1 \mu\text{M}$  tetrodotoxin (TTX) but were blocked by  $50 \mu\text{M}$   $\text{Ni}^{2+}$ , showing that they were mediated by T-type  $\text{Ca}^{2+}$  channels<sup>22</sup> (Fig. 3a–c).  $\text{Ca}^{2+}$  spikes in newly generated neurons had a voltage threshold of  $-56.0 \pm 1.2 \text{ mV}$  and an amplitude of  $17.6 \pm 1.1 \text{ mV}$  measured from the voltage at the end of the pulse ( $n = 16$ ). Furthermore, they had a slow time course with a duration at half-maximal amplitude of  $87 \pm 8 \text{ ms}$  ( $n = 16$ ). Thus, young granule cells generate low-threshold  $\text{Ca}^{2+}$  spikes under physiological conditions, whereas mature granule cells produce low-threshold  $\text{Ca}^{2+}$  spikes only in the presence of  $\text{K}^+$ -channel blockers<sup>23</sup>.

To examine whether the activation of T-type  $\text{Ca}^{2+}$  channels in young neurons contributed to the initiation of fast  $\text{Na}^+$  action potentials, we determined the probability of  $\text{Na}^+$  action potential initiation during current pulses of incremental amplitudes (Fig. 3d, e). A concentration of  $50 \mu\text{M}$   $\text{Ni}^{2+}$  markedly elevated the current threshold for the initiation of fast  $\text{Na}^+$  action potentials (Fig. 3e). On average, the current corresponding to the mid-point of the threshold curves increased to  $176 \pm 56\%$  of the control value in young neurons ( $n = 6$ ,  $P < 0.05$ ). By contrast, the threshold remained unchanged in mature neurons ( $98 \pm 3\%$ ,  $n = 4$ ). In conclusion, newly generated immature granule cells show a unique